PCCP

ROYAL SOCIETY OF CHEMISTRY

PAPER

Check for updates

Cite this: *Phys. Chem. Chem. Phys.*, 2025, **27**, 25462

Enhancing hydrogen adsorption on SnS_2 and $SnSe_2$ monolayers: alkali and alkaline earth metal decoration under external electric fields

Audomsak Sripothongnack,[a] Watcharin Teeranattapong,[a] Supparat Charoenphon,[a] Adisak Boonchun,[a] Thanayut Kaewmaraya[b] and Pakpoom Reunchan *[a]

Received 7th October 2025,
Accepted 11th November 2025

DOI: 10.1039/d5cp03873a

rsc.li/pccp

Efficient hydrogen storage is essential for advancing clean energy technologies. In this study, based on density functional theory (DFT), we report the hydrogen storage functionality of the post-transition metal dichalcogenides including SnS_2 and $SnSe_2$ monolayers modified by decoration with alkali (Li, Na, K) and alkaline-earth (Mg, Ca) metals. We reveal that Ca-decorated SnS_2 and $SnSe_2$ offer the most favorable hydrogen adsorption, with binding energies of approximately −0.15 eV per H_2 *via* strong physisorption. These systems can accordingly achieve the maximum gravimetric storage capacities ranging from 2.67 to 4.64 wt%. We further assess the key practical parameters relevant to storage capacities, including pressure, desorption temperature, and the influence of an external electric field. At a hydrogen pressure of 100 bar, the desorption temperatures for Ca–SnS_2 and Ca–$SnSe_2$ are calculated to be ∼226 K and ∼229 K, respectively. These values particularly approach the lower operational threshold of proton exchange membrane (PEM) fuel cells (∼233 K). Additionally, the desorption temperatures can be controllably modulated by 10–20 K through the application of a −0.5 V $Å^{-1}$ electric field, a typical magnitude in gated device structures. This tunability arises from field-induced variations in surface polarity, which influence H_2 binding energetics. Our findings highlight post-transition metal dichalcogenides as promising candidates for hydrogen storage, offering tunable performance through metal doping and external electric field control.

1. Introduction

The global transition toward sustainable energy has positioned hydrogen as a promising clean energy carrier capable of significantly reducing carbon emissions.[1] With its high gravimetric energy density and water as its only byproduct, hydrogen offers a compelling alternative to fossil fuels.[2,3] However, safe, efficient, and economically viable hydrogen storage remains a key challenge. Conventional storage methods—such as high-pressure gas cylinders and cryogenic tanks—not only pose safety risks but also require substantial energy input, limiting the practicality and scalability of hydrogen-based energy systems.[4] These challenges have spurred intensive research into solid-state hydrogen storage materials that promise more stable, compact, and safer solutions.[5]

Two-dimensional (2D) materials have emerged as attractive candidates for solid-state hydrogen storage due to their large surface areas, reduced dimensionality, and tunable electronic properties.[6–9] For instance, carbon-based materials like graphene, porous graphene, and carbon nanotubes have shown enhanced hydrogen adsorption when decorated with metals.[8,10–13] Similarly, carbon–nitride frameworks (*e.g.*, C_2N, C_3N)[14–16] and other 2D systems such as boron carbon–nitride,[17] borophene,[18] silicene,[19] and BeN_4[20–22] have demonstrated promise not only for hydrogen but also for other gas-molecule adsorption.[23,24] Despite these advances, many 2D materials still do not achieve the optimal hydrogen binding energies necessary for practical storage applications.

Recently, transition metal dichalcogenides (TMDs) have gained attention as potential platforms for hydrogen evolution[25,26] and storage.[27,28] Well-known for their catalytic, electronic, and optoelectronic properties, TMDs such as MoS_2 and WS_2 typically exhibit weak interactions with H_2 molecules in their pristine form, resulting in limited hydrogen uptake.[27] Metal atom decoration—particularly with alkali and alkaline-earth metals—has been proposed as a strategy to overcome this limitation.[28–30] The metal atoms donate electrons to the TMD substrate, thereby modifying its local electronic structure to create more favorable adsorption sites for hydrogen molecules, enhancing binding energies and charge transfer interactions.

[a] *Department of Physics, Faculty of Science, Kasetsart University, Bangkok 10900, Thailand. E-mail: pakpoom.r@ku.ac.th*
[b] *Department of Physics, Faculty of Science, Khon Kaen University, Mueang Khon Kaen, Khon Kaen 40002, Thailand*

 This journal is © the Owner Societies 2025

In addition to hydrogen-related applications, recent density functional theory (DFT) studies have demonstrated that 2D transition metal dichalcogenides (TMDs) such as MoS_2 and WSe_2 exhibit tunable electrochemical behavior under external electric fields, showing strong ion adsorption, excellent structural stability, and reduced diffusion barriers for charge carriers.[31] These results further emphasize that surface modification and field effects can significantly tailor the adsorption energetics and charge-transport characteristics in 2D TMD systems, providing valuable benchmarks for investigating post-transition-metal dichalcogenides like SnS_2 and $SnSe_2$.

Beyond these conventional TMDs, recent DFT studies have demonstrated that metal or cluster decoration can substantially modify hydrogen-related activity on 2D surfaces. For example, Au-cluster-decorated MoS_2 exhibits nearly thermoneutral hydrogen adsorption free energy and enhanced electronic transport properties relevant to hydrogen electrocatalysis, emphasizing how surface decoration tunes H–surface interactions and charge transfer on TMDs.[32]

In this study, we focus on SnS_2 and $SnSe_2$ monolayers, two members of the TMD family that have received limited attention for hydrogen storage applications. Experimentally, the synthesis of SnS_2 and $SnSe_2$ monolayers has been successfully demonstrated using techniques such as chemical vapor deposition (CVD), vapor-phase deposition, and molecular beam epitaxy (MBE).[33–36] For instance, high-quality $SnSe_2$ monolayers with excellent uniformity and crystallinity have been fabricated using CVD, highlighting their potential for practical applications.[33] In addition, exfoliation methods have also been employed to isolate monolayer and few-layer SnS_2 and $SnSe_2$, leveraging their intrinsic layered structure and weak interlayer van der Waals interactions.[36] These well-established synthesis routes provide strong experimental support for the viability of SnX_2 monolayers as a platform for further surface modification and functionalization. While direct experimental reports of metal-atom decoration on SnX_2 specifically for hydrogen storage are currently limited, the successful synthesis and stability of these monolayers suggest that such functionalization is feasible.

While SnX_2 monolayers share the layered structure of conventional TMDs, their electronic properties and interaction with hydrogen can be significantly modified by metal decoration. These materials have been more extensively studied for applications such as Na-ion battery anodes[37–39] and gas sensors,[40,41] and for tuning their electronic and optical properties through structural modifications.[35,42] Due to several key advantages, alkali (Li, Na, K) and alkaline-earth (Mg, Ca) metals were selected as decorating elements. First, these metals are lightweight, which helps maintain a low overall system mass—an essential criterion for achieving favorable gravimetric hydrogen storage capacity.[43–45] Second, their relatively low cohesive energies reduce the likelihood of metal clustering on the substrate, improving the stability and dispersion of single metal atoms on the SnX_2 surface.[10,46] Third, these metals readily donate electrons to the substrate, modifying the local charge distribution and creating favorable adsorption sites for molecular hydrogen through polarization and electrostatic interactions.[46,47] Collectively, these properties make alkali and alkaline-earth elements excellent candidates for enhancing hydrogen adsorption in 2D materials. Here, we use density functional theory (DFT) calculations to systematically investigate the effects of alkali and alkaline-earth metal decoration on hydrogen adsorption in SnS_2 and $SnSe_2$ monolayers.

To assess the practical viability of these materials for hydrogen storage, we further examine the influence of temperature, pressure, and external electric fields on hydrogen adsorption and desorption. The Gibbs free energy of adsorption is evaluated to determine the stability of hydrogen adsorption under realistic operating conditions, such as those required for proton exchange membrane (PEM) fuel cells. Additionally, the impact of an external electric field is explored to tune adsorption properties, offering a potential strategy for improving hydrogen storage performance. Our findings provide valuable insights into the adsorption behavior, thermodynamic stability, and tunability of metal-decorated SnS_2 and $SnSe_2$ monolayers for hydrogen storage applications. This study establishes a foundation for advancing experimental and theoretical approaches to optimize 2D materials for clean energy technologies by identifying crucial factors influencing hydrogen adsorption. The findings emphasize the promise of SnS_2 and $SnSe_2$ monolayers as adjustable platforms for next-generation solid-state hydrogen storage devices, offering theoretical insights that may inform future experimental efforts for effective energy storage applications.

2. Computational details

Our first-principles calculations were performed using density functional theory (DFT) implemented in the Vienna *ab initio* Simulation Package (VASP).[48,49] The projector augmented-wave (PAW) method described the interactions between core and valence electrons. The exchange–correlation interactions were treated using the Perdew–Burke–Ernzerhof (PBE) functional within the generalized gradient approximation (GGA).[50] To consider van der Waals (vdW) interactions, we utilized the DFT-D3 method with Becke–Johnson damping proposed by Grimme.[51] In some systems, we also tested other approaches that account for vdW interactions, such as DFT-D2,[52] DFT-D4,[53] and the Tkatchenko–Scheffler method,[54] including another functional, *i.e.*, local-density approximation (LDA), which was also used to investigate H_2 adsorption on the graphene and related materials as for comparison with the GGA functionals.[55,56] For all calculations, a plane-wave energy cutoff of 500 eV was applied. The Brillouin zone integrations utilized a Monkhorst–Pack k-point mesh of $12 \times 12 \times 1$ for the primitive unit cell calculations and $3 \times 3 \times 1$ for the supercell. A $3 \times 3 \times 1$ supercell was used for metal binding and H_2 adsorption studies, ensuring adequate separation between periodic images. Structural relaxations were performed until the forces on each atom were less than 0.02 eV $Å^{-1}$, and the energy convergence criterion was set to 10^{-5} eV. A uniform field was applied perpendicular to the slab (along z) using the finite-field method

implemented in VASP[57] with dipole correction to avoid interactions between the periodically repeated images. A vacuum layer of 30 Å was applied in the normal direction to the monolayers to prevent interactions between layers.

3. Results and discussion

3.1 SnS_2 and $SnSe_2$ monolayers

In principle, both SnS_2 and $SnSe_2$, a family of TMDs (*e.g.*, MoS_2, $MoSe_2$, WS_2, and WSe_2), can exist in trigonal (1T) and hexagonal (2H) phases. Unlike 2H MoS_2 with a space group $P6_3/mmc$, the 1T phase of SnS_2 and $SnSe_2$, with the space group notation of $P\bar{3}m1$ (no. 164), is energetically more stable than the 2H phase.[35,58] The monolayer structures comprise a layer of tin (Sn) atoms surrounded by two layers of chalcogen atoms (S or Se), creating a trigonal prismatic coordination around the Sn atoms, as shown in Fig. 1(a).

The structural and electronic properties of SnS_2 and $SnSe_2$ monolayers are summarized in Table 1. The lattice constants of 3.68 Å for SnS_2 and 3.84 Å for $SnSe_2$ reflect the larger atomic radius of selenium, with corresponding Sn–X bond lengths of 2.59 Å (SnS_2) and 2.73 Å ($SnSe_2$). These lattice constants and bond lengths are consistent with previously reported values.[35,37] We calculated the cohesive energy of the SnX_2 (where X = S, Se) monolayer using the following equation:

$$E_{coh} = \frac{E_{SnX_2} - (n_{Sn} \times E_{Sn} + n_X \times E_X)}{N}, \quad (1)$$

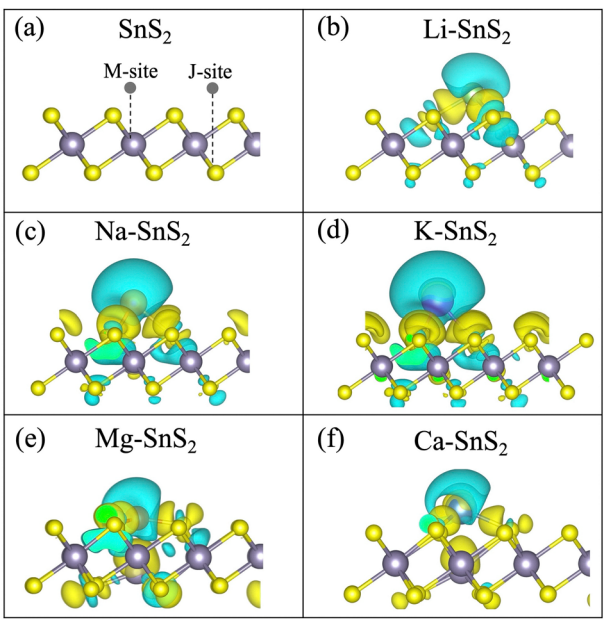

Fig. 1 Optimized atomic structures and charge difference distributions for pristine and metal-decorated SnS_2 monolayers. (a) Pristine SnS_2 monolayer showing the two potential adsorption sites: the M site (above the Sn atom) and the J site (above the lower-layer S atom). Panels (b)–(f) show the optimized structures of SnS_2 with adsorbed Li, Na, K, Mg, and Ca atoms, respectively, occupying the M site. The overlaid charge difference maps depict regions of charge accumulation (yellow) and charge depletion (blue), illustrating the redistribution of electron density upon metal adsorption (isosurface value is 20% of the maximum value).

Table 1 Calculated lattice parameters (a), cohesive energies (E_{coh}), Sn–X bond lengths (d_{Sn-X}, X = S, Se), thickness (d_{thick}), and band gaps (E_g) for SnS_2 and $SnSe_2$ monolayers

Property	SnS_2	$SnSe_2$
a (Å)	3.68	3.84
d_{Sn-X} (Å)	2.59	2.73
E_{coh} (eV per atom)	−3.68	−3.36
d_{thick} (Å)	2.96	3.19
E_g (eV)	1.57	0.77

where E_{SnX_2} is the total energy of SnX_2 monolayer, n_{Sn}, and n_X are the total numbers of tin (Sn), and chalcogens (S, Se) atoms in the monolayer. E_{Sn}, and E_X denote the energies of isolated Sn and X atoms, respectively, and N is the total number of atoms of the monolayer. The cohesive energies of −3.68 eV per atom for SnS_2 and −3.36 eV per atom for $SnSe_2$ indicate that SnS_2 is slightly more stable.

In addition, the phonon dispersion spectra exhibit no imaginary frequencies across the Brillouin zone for either SnS_2 or $SnSe_2$, demonstrating that both monolayers are dynamically stable (see SI, Fig. S1). This finding confirms their structural robustness and supports their feasibility as candidates for hydrogen storage applications.

Our GGA-PBE calculated band gaps are underestimated compared to HSE results, but align well with previously reported values.[37] According to HSE06 hybrid functional calculations, SnS_2 has a wider indirect band gap of approximately 2.40 eV,[35] which is characteristic of semiconductors with relatively low electrical conductivity due to limited thermally excited charge carriers at room temperature.

Conversely, $SnSe_2$ possesses a narrower indirect band gap of about 1.41 eV,[35] implying enhanced electrical conductivity. The smaller band gap allows more electrons to be thermally excited from the valence band to the conduction band, increasing the intrinsic carrier concentration. This significant difference in band gap sizes influences their electronic properties during adsorption processes. The higher conductivity of $SnSe_2$ may facilitate better charge transfer interactions with adsorbates like hydrogen molecules, potentially improving adsorption performance and making it a more favorable candidate for hydrogen storage applications.

3.2 Adsorption of metal atoms on SnS_2 and $SnSe_2$ monolayers

Decorating two-dimensional (2D) materials with metal atoms is a promising strategy to enhance their hydrogen storage capabilities by introducing active sites and modifying electronic properties. Here, we investigate the adsorption behavior of alkali metals (Li, Na, K) and alkaline earth metals (Mg, Ca) on SnS_2 and $SnSe_2$ monolayers using DFT-D3 calculations. Understanding the binding characteristics and stability of these metal atoms on the monolayer surfaces is crucial for evaluating their potential as efficient hydrogen storage materials.

The metal binding energy (E_{bind}) was calculated to assess the interaction between the metal atoms and the SnS_2 or $SnSe_2$ monolayers. The binding energy is defined as:

$$E_{bind} = E_{M-SnX_2} - (E_{SnX_2} + E_M), \quad (2)$$

This journal is © the Owner Societies 2025

where E_{M-SnX_2} is the total energy of the SnX_2 monolayer with an adsorbed metal atom M, and E_{SnX_2} is the total energy of the pristine SnX_2 monolayer. E_M is the total energy of an isolated metal atom M. A negative value of E_{bind} indicates that the adsorption of the metal atom onto the monolayer is exothermic and energetically favorable. We examined two potential adsorption sites for metal atoms on SnX_2: (i) the site located directly above the Sn atom, positioned at the center of the equilateral triangle formed by the upper layer of S atoms, and (ii) the site directly above the X atoms in the bottom layer. These sites are commonly referred to as the M site (above the Sn atom) and the J site (above the lower X atoms), following designations used in previous studies.[37] Based on our calculated binding energies in Table S1, all examined metal atoms exhibit a clear preference for binding at the M site rather than the J site on both SnS_2 and $SnSe_2$ monolayers. Specifically, the calculated binding energies at the M site are consistently lower (more negative) than those at the J site, indicating stronger metal–substrate interactions. The only exceptions occur for Li atoms on SnS_2 and $SnSe_2$, and Na atoms on SnS_2, where the metal atoms remain bound to the J site after geometry optimization. Nevertheless, even in these cases, the binding energies at the M and J sites are very close, reflecting a subtle balance of stability between the two positions. Furthermore, the calculated binding energies are significantly more negative than the corresponding cohesive energies of these metals, confirming that isolated metal atoms will preferentially bind to the SnS_2 and $SnSe_2$ surfaces rather than forming metal clusters. Moreover, formation energies defined as $E_{form} = E_{M-SnX_2} - E_{SnX_2} - \mu_M$ where μ_M is the chemical potential referenced to the metal atom in the bulk on SnX_2, are all negative, confirming that the metal atoms are thermodynamically stable when adsorbed on SnX_2 surfaces, as shown in Table S2.

Fig. 1(a) shows the pristine SnS_2 structure with M and J sites labeled, while panels (b) through (f) display the optimized structures of SnS_2 with Li, Na, K, Mg, and Ca adsorbed at the M site. The accompanying charge density difference (CDD) distributions ($\Delta\rho$) illustrate regions of charge accumulation (yellow) and charge depletion (blue) due to metal adsorption. These charge distributions help us understand the electronic interactions between the adsorbed metals and the SnS_2 surface, providing insight into the strength and nature of the metal–SnS_2 bonds. A similar illustration for pristine and metal-decorated $SnSe_2$ is shown in Fig. S2 in the SI.

The charge difference maps in Fig. 1 reveal distinct charge redistribution patterns for each metal. We observe moderate charge accumulation around the metal atoms for Li and Na (Fig. 1(b) and (c)), indicating relatively weak but stable binding. In contrast, K (Fig. 1d) shows less pronounced charge accumulation, consistent with its relatively weak binding energy on SnS_2, as discussed earlier. This weaker binding is further evidenced by the larger K–S distance compared to Li and Na, suggesting K interacts less strongly with the SnS_2 surface.

For the alkaline-earth metals, Mg and Ca (Fig. 1(e) and (f)), the charge difference maps show significant charge redistribution, particularly around Ca. The charge accumulation around Ca is more pronounced than Mg, reflecting Ca's higher binding energy. This suggests that Ca forms a more stable and stronger interaction with the SnS_2 surface than the other studied metals. The Bader charge analysis in Table 2 shows that the relatively high charge transfer from Ca to the SnS_2 monolayer further supports this strong binding interaction.

Table 2 Summarizes the average metal–chalcogen bond distances and the Bader charge (Q_M) on the metal atoms adsorbed on SnS_2 and $SnSe_2$ monolayers

Metal	d_{M-S} (Å)	d_{M-Se} (Å)	Q_{M-SnS_2} (e)	Q_{M-SnSe_2} (e)
Ca	2.649	2.760	+1.013	+0.859
K	3.126	3.233	+0.783	+0.714
Li	2.431	2.531	+0.416	+0.350
Mg	2.408	2.527	+0.618	+0.494
Na	2.751	2.863	+0.671	+0.492

The binding energies for these metal atoms, presented in Fig. 2, reveal distinct trends across both monolayers. The binding energies are generally more negative for $SnSe_2$ than SnS_2, indicating stronger interactions with $SnSe_2$. The results indicate that all metal atoms exhibit strong exothermic adsorption on SnS_2 and $SnSe_2$ monolayers. Among the alkali metals, Li shows the most negative binding energies, suggesting the most potent interaction with the monolayers. Calcium exhibits the most negative binding energies for the alkaline earth metals, indicating a robust adsorption affinity. Comparatively, the binding energies on $SnSe_2$ are slightly more negative than those on SnS_2 for all metals studied, suggesting that $SnSe_2$ may interact more strongly with metal atoms than SnS_2.

To assess the likelihood of metal atom clustering on the monolayer surfaces, we compare the calculated binding energies to the cohesive energies (E_{coh}) of the corresponding bulk metals, as shown in Fig. 2. For all metal atoms, the binding energies on both monolayers are more negative than their respective cohesive energies ($E_{bind} < E_{coh}$). This indicates that it is energetically more favorable for the metal atoms to remain adsorbed on the monolayer surfaces rather than clustering to form bulk metal. For example, the binding energy of Ca on SnS_2 is −3.80 eV, which is significantly more negative than its cohesive energy of −1.98 eV. This thermodynamic preference for adsorption over clustering ensures a high dispersion of metal atoms on the monolayer surfaces, which is beneficial for maximizing hydrogen adsorption sites.

Interestingly, the bond distances between metals and Se are consistently longer than between metals and S, yet the binding energies are still more negative on $SnSe_2$. Moreover, the Bader charge analysis shows that the charge transfer from the metals to the monolayers is lower on $SnSe_2$ than on SnS_2. This suggests that factors such as electronic structure and lattice flexibility likely contribute to the stronger adsorption observed on $SnSe_2$ despite the longer bond distances and lower charge transfer.

To evaluate the thermal and structural stability under realistic operating conditions, we conducted *ab initio* molecular dynamics (AIMD) simulations for representative metal-decorated SnS_2 and $SnSe_2$ monolayers at 300 K for 10 ps. For single-metal-atom decoration, the AIMD results showed excellent structural

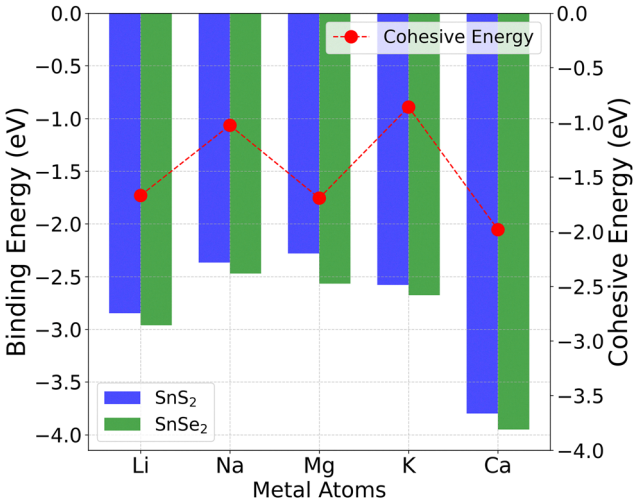

Fig. 2 Binding energies of alkali and alkaline-earth metals (Li, Na, Mg, K, Ca) adsorbed on SnS_2 (blue bars) and $SnSe_2$ (green bars) monolayers are compared with the cohesive energies of the metals (red circles). The dashed line only serves to guide the eyes.

integrity with negligible displacement of the decorated atoms, indicating robust adsorption sites and minimal risk of clustering or migration (see Fig. S3–S12 in SI). Thus, these structures demonstrate sufficient stability for practical hydrogen storage applications. However, upon increasing the decoration density to multiple metal atoms per supercell, only Li and Na decorations maintained structural stability with minimal distortion. Conversely, K, Mg, and Ca decorated systems exhibited noticeable structural distortions, although significantly, no metal atoms detached from the SnX_2 substrates. The observed structural distortions at higher coverages suggest that metal loading and distribution must be optimized for practical application. Strategies such as vacancy engineering, co-doping, or controlled placement of metal atoms could mitigate these issues, thereby enhancing structural robustness under realistic operational conditions.

3.3 Hydrogen adsorption on pristine and metal-decorated SnS_2 and $SnSe_2$

To establish a baseline for hydrogen uptake, we initially examined pristine SnS_2 and $SnSe_2$ monolayers. In these systems, H_2 molecules generally orient themselves above the Sn center (M-site). Our DFT calculations yield adsorption energies of approximately −0.051 eV for SnS_2 and −0.055 eV for $SnSe_2$, indicating slightly stronger H_2 binding in $SnSe_2$. These values are used as criteria to determine the maximum number of adsorbed H_2 molecules for each system in Table 4. Nevertheless, both values reflect weak physisorption, dominated by van der Waals interactions rather than substantial charge transfer. Such weak adsorption suggests that pristine SnS_2 and $SnSe_2$ alone are not optimal for hydrogen storage, underscoring the need for material engineering—such as metal decoration—to enhance adsorption energetics.

We subsequently investigated hydrogen adsorption on Li-, Na-, K-, and Ca-decorated SnS_2 and $SnSe_2$ monolayers, systematically placing H_2 molecules near the adsorbed metals. After optimizing each geometry. To comprehensively examine the adsorption configurations, several initial orientations of H_2 molecules were considered for each metal-decorated SnS_2 and $SnSe_2$ monolayer, including (i) parallel (side-on) to the surface, (ii) perpendicular (end-on) to the surface, and (iii) tilted orientations relative to the metal atom. The H_2 molecules were initially placed sufficiently far apart from one another to minimize intermolecular interactions. All configurations were fully relaxed without any geometric constraints, and the optimized H–H bond lengths (∼0.75–0.76 Å) confirm that the adsorption is dominated by weak physisorption rather than chemisorption, we calculated the consecutive adsorption energies to evaluate how each additional H_2 molecule modifies the binding environment. We define the consecutive adsorption energy E^n_{ads} for the n-th H_2 molecule as follows:

$$E^n_{ads} = E_{M+SnX_2+nH_2} - E_{SnX_2+M+(n-1)H_2} - E_{H_2}, \quad (3)$$

where $E_{M+SnX_2+nH_2}$ and $E_{SnX_2+M+(n-1)H_2}$ are the total energy of the metal-decorated SnX_2 monolayer with n and $n-1$ adsorbed H_2 molecules, respectively. E_{H_2} is the total energy of an isolated H_2 molecule in the gas phase.

Fig. 3 presents these adsorption energies for 1–5 H_2 molecules on (a) SnS_2 and (b) $SnSe_2$, with horizontal dotted lines indicating the adsorption energies of H_2 on the pristine monolayers. A few important trends emerge. First, the initially adsorbed H_2 molecules often exhibit more negative (*i.e.*, stronger) adsorption energies, typically falling in the range of about −0.15 to −0.20 eV per H_2 for certain metal dopants. These values lie between typical physisorption (below −0.10 eV) and chemisorption (often above −0.50 eV), suggesting a blend of interactions. Specifically, partial charge transfer from the decorated metal to the substrate creates localized charges or polarized sites on the surface, which can induce Coulombic (electrostatic) attraction and polarization effects in the H_2 molecules. While these mechanisms exceed the strength of purely non-specific van der Waals interactions, they do not amount to complete orbital

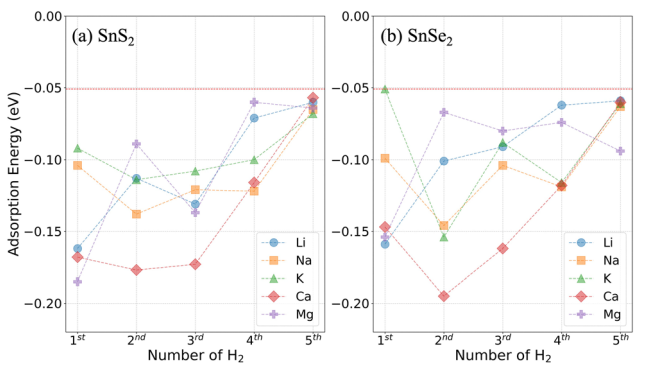

Fig. 3 Adsorption energies of individual H_2 molecules on metal-decorated (a) SnS_2 and (b) $SnSe_2$ monolayers. The adsorption energies are shown for up to five hydrogen molecules on surfaces decorated with Li (blue circles), Na (orange squares), K (green triangles), and Ca (red diamonds). The horizontal dotted lines show the adsorption energies of a H_2 molecule on pristine SnS_2 and $SnSe_2$.

This journal is © the Owner Societies 2025

hybridization or bond formation, placing the adsorption in the regime sometimes referred to as strong physisorption.

As additional H_2 molecules adsorb, Li and Na systems often experience a gradual decrease in adsorption energy, indicating a saturation effect or mutual repulsion between adsorbates. In contrast, Ca-decorated monolayers exhibit relatively consistent adsorption energies at higher coverages, highlighting their capacity to accommodate multiple H_2 molecules with a lower penalty in binding strength. Subtle differences between SnS_2 (Fig. 3(a)) and $SnSe_2$ (Fig. 3(b)) also appear—likely due to variations in their electronic structures. The overall trends remain similar. In both materials, Ca emerges as a standout dopant, balancing favorable H_2 adsorption with the ability to maintain exothermic adsorption across several molecules.

Fig. 4 shows the maximum-coverage configuration for Ca-decorated SnS_2 with five adsorbed H_2 molecules. Panels (a) and (b) present the side and top views of the CDD plots, revealing clear electron depletion around the Ca atom and accumulation on adjacent Sn–S bonds. This indicates that Ca donates charge to the substrate, while the H_2 molecules exhibit only weak polarization, with minor charge redistribution along the H–H axis but no charge accumulation between H and Ca. These results confirm that the H–H covalent bonds remain intact and that adsorption arises primarily from electrostatic polarization rather than covalent bonding. The optimized geometry shows H_2–Ca distances ranging from 2.73 Å to 3.35 Å (averaging ~3.0 Å), while the H–H bond length remains nearly unchanged at ~0.76 Å, consistent with strong physisorption. The average metal–H_2 distances and bond lengths across different decorated systems are summarized in Table 3.

Fig. 4(c) provides the corresponding density of states (DOS), decomposed into the Ca 3d (red) and H 1s (blue) contributions, with the dashed line representing the Fermi energy. The minimal overlap between these states corroborates the interpretation of a weakly chemisorbed or "enhanced physisorption" regime. The lack of significant new bonding peaks near the Fermi level further underscores that hydrogen remains physisorbed on the surface,

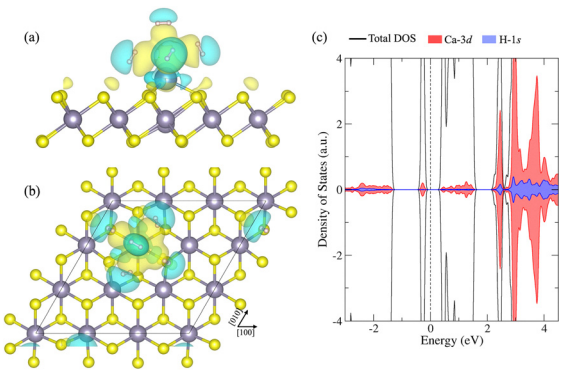

Fig. 4 (a) Side view and (b) top view of the charge density difference (CDD) distribution for Ca-decorated SnS_2 with five adsorbed H_2 molecules. Yellow and cyan regions denote charge accumulation and depletion, respectively (isosurface value is 5% of the maximum value). (c) Total and projected density of states (PDOS) showing contributions from Ca-3d (red) and H-1s (blue) orbitals. The dashed line indicates the Fermi energy.

Table 3 Average metal–H_2 distances (d_{M-H_2}) and H_2 bond lengths (d_{H_2}) for adsorbed H_2 on metal-decorated $SnSe_2$ and SnS_2 systems under 0.0 V Å^{-1} and −0.5 V Å^{-1} electric fields (E_f)

		d_{H_2} (Å)		d_{M-H_2} (Å)	
	Metal	E_f = 0.0	E_f = −0.5	E_f = 0.0	E_f = −0.5
$SnSe_2$	Ca	0.76	0.76	2.97	2.84
	K	0.75	0.75	3.09	3.02
	Li	0.75	0.76	2.62	2.53
	Mg	0.75	0.75	3.57	3.45
	Na	0.75	0.75	2.78	2.67
SnS_2	Ca	0.76	0.76	3.00	2.90
	K	0.75	0.75	3.07	3.03
	Li	0.75	0.75	3.04	2.89
	Mg	0.75	0.76	3.45	3.19
	Na	0.75	0.75	2.76	2.66

lacking the strong Kubas-type interactions observed in other systems (*e.g.*, Ca-decorated porous graphene).[10] Such moderate binding strengths are advantageous for hydrogen storage, enabling stable adsorption while maintaining the possibility of release under practical conditions. The maximum-coverage configurations, corresponding DOS, and CDD plots for other metal–SnX_2 systems are provided in the SI (Fig. S18–S26).

To further assess the viability of metal-decorated SnX_2 monolayers for hydrogen storage, Table 4 summarizes three key properties for each system: the maximum number of adsorbed H_2 molecules, the corresponding average adsorption energy per H_2, and the maximum gravimetric hydrogen capacity expressed in weight percent (wt%). We define the average adsorption energy ($\bar{E}_{ads}$) per H_2 when nH_2 molecules are adsorbed as

$$\bar{E}_{ads} = \frac{E_{M+SnX_2+nH_2} - E_{SnX_2+M} - nE_{H_2}}{n} \quad (4)$$

Since the decorating metal favors the M site (above the Sn atom), assuming that every Sn atom will serve as the binding site for two metal atoms (if both sides of the SnX_2 are decorated) is impractical. This is because the decorating metal atoms would be too close together, leading to metal clustering, significant host lattice distortion, or metal–SnX_2 separation. To estimate the maximum gravimetric capacity, we assume

Table 4 Maximum number of adsorbed H_2 (n_{max}), average adsorption energy ($\bar{E}_{ads}$), gravimetric hydrogen capacity, and volumetric for metal-decorated $SnSe_2$ and SnS_2 monolayers

	Metal	n_{max}	$\bar{E}_{ads}$ (eV)	GC_{max} (wt%)	C_v (g L^{-1})
SnS_2	Li	5	−0.107	4.65	55.09
	Na	5	−0.110	4.04	55.52
	K	5	−0.096	3.58	40.93
	Mg	5	−0.107	4.00	53.08
	Ca	5	−0.138	3.55	42.97
$SnSe_2$	Li	5	−0.094	3.24	52.80
	Na	5	−0.106	2.94	44.95
	K	5	−0.094	2.68	39.91
	Mg	5	−0.094	2.91	51.80
	Ca	5	−0.136	2.67	47.58

every two SnX_2 primitive cells may contain only two metal atoms (utilize both sides of SnX_2). We calculate the gravimetric capacity (GC) and volumetric capacity of hydrogen as:

$$\mathrm{GC\,(wt\%)} = \frac{2n_{H_2}W_H}{n_{Sn}W_{Sn} + n_X W_X + n_M W_M + 2n_{H_2}W_H} \times 100 \quad (5)$$

where n_{H_2}, n_{Sn}, n_X, and n_M is the number of adsorbed H_2 molecules, Sn, X, and metal atoms in the supercell. W_H, W_{Sn}, W_X, W_M are the atomic mass of H, Sn, X (S or Se), and metal, respectively.

$$C_v = \frac{m_{H_2}}{V}, \quad (6)$$

where m_{H_2} represents the mass of stored hydrogen and V denotes the system volume.

For $SnSe_2$ and SnS_2, most decorated surfaces can accommodate up to five hydrogen molecules per metal site, except for Li on $SnSe_2$, which saturates at four H_2. While five is the most common upper limit across the systems studied, this difference suggests that Li on $SnSe_2$ may reach a point of steric or electronic saturation slightly sooner than the other metals. The average adsorption energies, ranging approximately from −0.094 eV (Mg on $SnSe_2$) to −0.136 eV (Ca on $SnSe_2$), place these systems in the strong physisorption regime. This energy range implies that hydrogen remains stably bound yet can still be released under moderate conditions without extreme difficulty. Notably, Ca on $SnSe_2$ shows the most negative average adsorption energy (−0.136 eV), which correlates well with Ca's tendency to donate charge and form moderately strong electrostatic interactions with H_2.

It is crucial to recognize that the computed adsorption energies depend on the chosen exchange–correlation functional and van der Waals treatment. Our test calculations shown in Fig. 5 illustrate that the computed adsorption energies of H_2 molecules on Li-decorated SnS_2 and $SnSe_2$ are sensitive to the chosen exchange–correlation functional and van der Waals treatment. Notably, DFT-D2 and LDA predict more negative (*i.e.*, stronger) adsorption energies than the other methods, implying a higher theoretical hydrogen storage capacity. However, it is well-known that both DFT-D2 and LDA can overestimate binding by ascribing too much weight to short-range correlation effects. In contrast, more advanced schemes (*e.g.*, DFT-D3, DFT-D4, and Tkatchenko–Scheffler) are often considered more balanced for physisorption-dominated systems. Without direct experimental measurements on Li-decorated SnS_2 or $SnSe_2$, there is no definitive "true" adsorption energy for comparison. Consequently, these results highlight both the flexibility and the uncertainty of computational predictions: different dispersion corrections can shift the estimated adsorption energies—and hence apparent storage efficiencies—by tens of meV per H_2. This underlines the importance of carefully benchmarking computational approaches and emphasizes the need for complementary experimental studies to validate which method best captures the actual adsorption behavior in these 2D materials.[12,18,22,59] We noted that several recent DFT calculations related to the adsorption of H_2 on metal-decorated 2D materials employed the DFT-D2 method to correct for van der Waals dispersion. If we use the DFT-D2 method for this correction, our calculated average H_2 adsorption energy on metal-decorated SnX_2 monolayers in this work is expected to be more negative (indicating stronger adsorption) by several meV per H_2. Our calculated adsorption energies for H_2 adsorption on alkaline and alkaline-earth metal-decorated SnX_2 are comparable to other widely studied 2D materials decorated with alkaline or alkaline-earth metals, such as graphene and its derivatives (*e.g.*, porous graphene,[10] defective graphene,[60] and Ψ-graphene[61]), graphitic carbon nitride (C_3N, C_2N)[46,62]), which adopted different levels of van der Waals dispersion. Our results for Li decorated SnX_2 using DFT-D2 yield higher H_2 adsorption energy than DFT-D3, DFT-D4, and Tkatchenko–Scheffler dispersions (Fig. 5). The adsorption energies match well with those obtained by DFT-D2 in Li-decorated 2D systems.

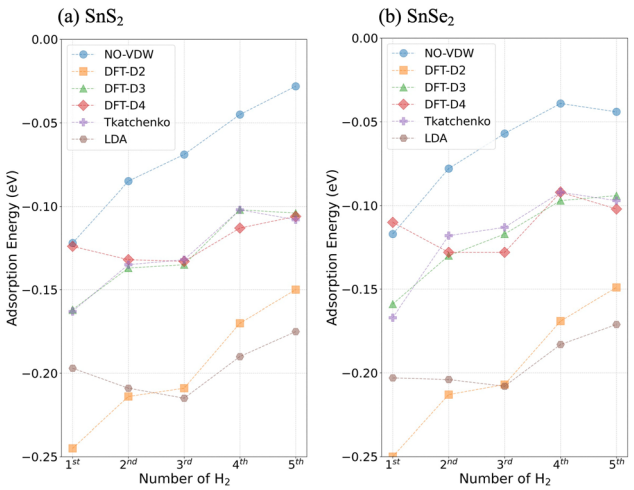

Fig. 5 Comparison of the average H_2 adsorption energies on Li-decorated (a) SnS_2 and (b) $SnSe_2$ using different van der Waals treatments and functional (*e.g.*, DFT-D2, DFT-D3, DFT-D4, Tkatchenko–Scheffler, and LDA).

Regarding gravimetric capacity, the SnS_2-based systems consistently exhibit higher weight percentages than their $SnSe_2$ counterparts, mainly due to the lower atomic mass of sulfur compared to selenium. For example, Li-decorated SnS_2 achieves approximately 4.65 wt%, whereas Li-decorated $SnSe_2$ reaches only 3.24 wt%. Although these values remain below stringent benchmarks, such as those set by the U.S. Department of Energy for on-board applications, they underscore the pronounced influence of both metal dopants and chalcogen composition on hydrogen uptake. This finding highlights potential avenues for further material optimization to bridge the gap toward practical hydrogen storage.

Although the calculated gravimetric capacities (up to ∼4.65 wt%) do not meet current Department of Energy (DOE) benchmarks for on-board hydrogen storage, these findings offer key insights into how metal dopants and chalcogen composition influence adsorption energetics. By pinpointing factors such as electron donation, weak chemisorption, and substrate-dependent charge redistribution, this study provides

 This journal is © the Owner Societies 2025

Table 5 Comparison of gravimetric hydrogen storage capacities predicted from DFT calculations for various metal-decorated two-dimensional materials. The applied van der Waals correction scheme used to account for weak dispersion interactions is also indicated

System	Van der Waals correction	Gravimetric capacity (wt%)	Ref.
$Li@C_6O_6Li_6$-$4H_2$	DFT-D3	10.00	63
$Na@C_6O_6Li_6$-$5H_2$		9.52	
$K@C_6O_6Li_6$-$6H_2$		9.75	
$Y@MoS_2$	DFT-D2	4.56	29
$Li@MoS_2$	DFT-D2	4.4	64
$1T'$-$WS_2(H_2)$	LDA (no vdW)	2.7	65
2H-$WS_2(H_2)$		2.4	
$Li@SnS_2$-$5H_2$	DFT-D3	4.65	This work
$Na@SnS_2$-$5H_2$		4.04	This work
$Ca@SnS_2$-$5H_2$		3.55	This work

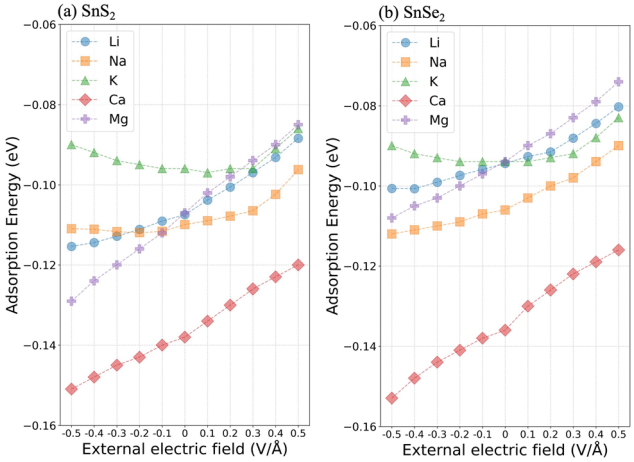

Fig. 6 Adsorption energy of H_2 molecules as a function of the external electric field (−0.5 V Å^{-1} to +0.5 V Å^{-1}) for metal-decorated (a) SnS_2 and (b) $SnSe_2$ monolayers. Results are shown for Li (blue circles), Na (orange squares), K (green triangles), Mg (purple crosses), and Ca (red diamonds).

a valuable framework for targeted material optimization. Future efforts—such as co-doping, strain engineering, or external field application—could further elevate both adsorption energies and capacities, bridging the gap toward practical hydrogen storage while preserving reversibility and manageable operating conditions. To further contextualize the performance of our systems, Table 5 compares the gravimetric hydrogen capacities obtained in this work with those reported for other 2D hydrogen-storage materials.

3.4 Effects of external electric field on H_2 adsorption

Applying an external electric field to metal-decorated materials has been previously shown to effectively tune H_2 adsorption energies by enhancing polarization-induced electrostatic interactions between the adsorbed hydrogen molecules and substrate atoms.[47,66,67] It has been demonstrated that substrates such as metal-decorated graphene and BN sheets significantly enhance their hydrogen storage capabilities under an applied electric field, primarily due to increased polarization of H_2 molecules and substrate atoms, resulting in stronger adsorption interactions. Inspired by these findings, we systematically investigate how external electric fields influence the H_2 adsorption behavior on alkali- and alkaline-earth metal-decorated SnS_2 and $SnSe_2$ monolayers.

In this study, the applied electric field is imposed in the perpendicular direction, either downward (negative values) or upward (positive values), to the metal-decorated SnS_2 and $SnSe_2$ monolayers. The dispersion correction (DFT-D3) for van der Waals interactions was also included in the calculations for H_2 adsorption energy.

Fig. 6(a) and (b) illustrate the variation in adsorption energy per H_2 molecule as a function of external electric field strength for metal-decorated SnS_2 and $SnSe_2$ monolayers. Across all systems, the adsorption energies become more negative under negative electric fields (−0.5 V Å^{-1}) and less negative under positive fields (+0.5 V Å^{-1}), demonstrating that external fields can modulate the interaction strength. This trend is attributed to charge redistribution effects at the dopant–H_2 interface, where negative fields enhance polarization-driven stabilization while positive fields reduce it. Among the dopants, Ca consistently exhibits the most negative adsorption energies, highlighting its strong interaction with H_2 and its potential for field-tunable applications.

The observed increase in adsorption energy under a negative external electric field can be attributed to the polarization of H_2 molecules. As shown in Table 3, the H_2–metal distances decrease under the −0.50 V Å^{-1} field for all systems, with reductions ranging from 0.04 Å (K on SnS_2) to 0.25 Å (Mg on SnS_2). This reduction indicates that the induced dipole moment in the H_2 molecule strengthens its electrostatic interaction with the decorated metal atom on the SnX_2 monolayer. For example, in the case of Ca on $SnSe_2$, the H_2–metal distance decreases from 2.97 Å to 2.84 Å under the field, highlighting how the field enhances attraction between the polarized H_2 molecule and the metal dopant. Despite this closer interaction, the H_2 bond length remains largely unaffected, with values consistently around 0.75–0.76 Å across all systems, suggesting that the molecule retains its structural integrity. This polarization-driven reduction in equilibrium distance increases the overlap between the molecule's electron cloud and the local electrostatic potential, leading to more negative adsorption energies and stronger binding. These results underscore the role of external electric fields in fine-tuning hydrogen adsorption properties by modulating dipole-induced interactions and adsorption distances.

To assess the thermal and field-induced stability, *ab initio* molecular dynamics (AIMD) simulations were performed at 300 K under an external electric field of −0.5 V Å^{-1} for 10 ps. The results reveal that decoration on both sides or at higher adatom densities leads to noticeable adatom–adatom interactions and surface distortions, as evidenced by increased total energies and unstable AIMD trajectories. These effects are most pronounced for the Mg–SnX_2 systems, which undergo structural deformation during thermal-field simulations, whereas other metal–SnX_2 systems (Li, Na, K, and Ca) remain structurally stable (Fig. S13–S17). Such behavior suggests that

excessive Mg loading could reduce the achievable hydrogen storage capacity by destabilizing the host lattice under realistic operating conditions.

The sensitivity of adsorption energies to the electric field is metal-specific, with more substantial effects observed for Ca and Li compared to K and Mg. SnS_2 generally provides stronger binding than $SnSe_2$ for all dopants, though the relative trends remain consistent. The ability to modulate adsorption energies by ~0.05–0.10 eV with realistic electric fields underscores the utility of this approach for tuning hydrogen storage and release. These findings highlight the promise of combining metal decoration with external electric field control for next-generation hydrogen storage systems.

4. Thermodynamic stability: effect of temperature and pressure

To access the practical hydrogen storage capability of the SnX_2 monolayers, we consider the effects of temperature and pressure on the adsorption and desorption of the stored hydrogen through the average Gibbs free energy ($\Delta\bar{G}_{ads}$) of the adsorbed H_2 molecule, defined as

$$\Delta\bar{G}_{ads} = E_{M+SnX_2+nH_2} - E_{SnX_2+M} - n[E_{H_2} + \mu_{H_2}(T,P)], \quad (7)$$

where $E_{M+SnX_2+nH_2}$, E_{SnX_2+M}, and E_{H_2} are the total energy of the metal-decorated SnX_2 with n adsorbed H_2 molecules, the metal-decorated SnX_2 without adsorbed H_2 molecules, and the isolated H_2 molecule, respectively. The effects of temperature (T) and pressure (P) are included in the chemical potential of the H_2 molecule $\mu_{H_2}(T,P)$ as follows,

$$\mu_{H_2}(T,P) = \Delta H - T\Delta S + k_B T \ln\left(\frac{P}{P_0}\right) \quad (8)$$

where ΔH and ΔS are the changes of enthalpy and entropy of hydrogen, derived from the thermochemical tables of hydrogen in the gas phase.[18,68] P_0 and k_B denote the standard atmospheric pressure (0.1 MPa) and the Boltzmann constant. Fig. 7 represents the temperature dependence of $\Delta\bar{G}_{ads}$ for 1–5 H_2 molecules adsorbed on Ca-decorated SnS_2 at three different pressures: (a) 0.1 MPa, (b) 1 MPa, and (c) 10 MPa. A negative $\Delta\bar{G}_{ads}$ indicates that the H_2 adsorbed system is thermodynamically favorable, while positive values suggest spontaneous desorption.

According to the United States Department of Energy (DOE), the desorption temperature of polymer electrolyte membrane (PEM) fuel cells is influenced by the operating temperature of the proton exchange membrane, which typically ranges from approximately 233 to 473 K[69] or, depending on the specific design of the cell, from 270 to 390 K.[70] The typical operating pressure of a PEM fuel cell is approximately 3 bars (0.3 MPa) of H_2 pressure, meaning that the storage material needs to maintain a higher H_2 pressure to supply H_2 to the fuel cell effectively. Additionally, a maximum limit of 100 bars (10 MPa) has been suggested for the H_2 vapor to prevent similar technological issues as those encountered with pressurized gas containment.

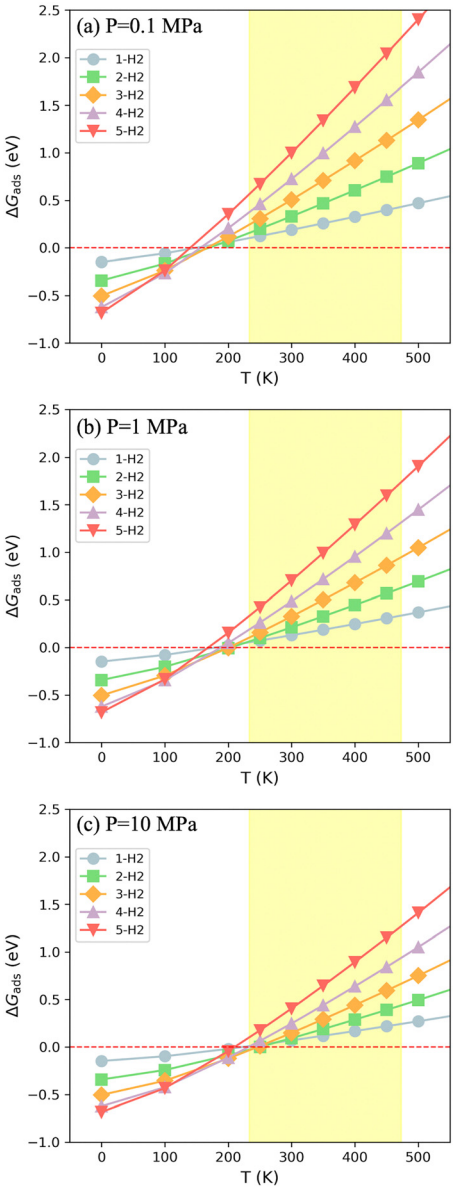

Fig. 7 Average Gibbs free energy of nH_2 adsorbed on Ca-decorated SnS_2 under (a) standard atmospheric pressure, P = 0.1 MPa, (b) P = 1 MPa, and (c) P = 10 MPa. The shaded area indicates the operating temperature of the fuel cell (233–473 K).

At low pressure (0.1 MPa), the calculated desorption temperatures ($T_{\Delta G=0}$) for Ca-decorated SnS_2 range from 141 K to 171 K across all coverages (n = 1–5), with single H_2 adsorption (n = 1) being slightly more stable ($T_{\Delta G=0} \approx 167$ K). Desorption occurs at progressively lower temperatures for higher H_2 coverages (n = 2–5). Similarly, for $SnSe_2$, the desorption temperatures range from 140 K ($5H_2$) to 170 K ($2H_2$), indicating weak binding similar to SnS_2 (see Table S3 in the SI). The low desorption temperatures at 0.1 MPa underscore the inability of Ca-decorated SnX_2 to retain hydrogen at temperatures relevant for practical applications, such as PEM fuel cells, which typically operate between 233 K and 473 K. This suggests that higher pressures are essential for stabilizing hydrogen adsorption.

This journal is © the Owner Societies 2025

At moderate pressure (1 MPa), the desorption temperatures increase significantly, providing improved thermodynamic stability. For SnS_2, $T_{\Delta G=0}$ ranges from 171 K ($5H_2$) to 205 K ($2H_2$), with single H_2 adsorption (n = 1) remaining stable up to ~201 K. In $SnSe_2$, the desorption temperatures also improve, ranging from 168 K ($5H_2$) to 203 K ($2H_2$). Although adsorption stability improves compared to 0.1 MPa, the desorption temperatures are still below the operational range of PEM fuel cells, limiting the utility of Ca-decorated SnS_2 and $SnSe_2$ at moderate pressures.

At high pressure (10 MPa), the desorption temperatures shift into a range more suitable for practical applications. For SnS_2, $T_{\Delta G=0}$ ranges from 212 K ($5H_2$) to 252 K ($2H_2$), with single H_2 adsorption (n = 1) stable up to ~246 K. Similary, for $SnSe_2$, $T_{\Delta G=0}$ ranges from 210 K ($5H_2$) to 250 K ($2H_2$). At this pressure, the system can maintain thermodynamically favorable adsorption up to the lower end of the PEM fuel cell operating range (~233 K). These results suggest that Ca-decorated SnS_2 can store hydrogen effectively under high-pressure conditions, meeting the DOE's operational pressure limit of 10 MPa. However, the desorption temperatures for higher H_2 coverages (n = 3–5) remain near or below the PEM operating range, highlighting the need for additional optimization.

5. Effect of external electric fields on desorption temperatures

According to Section 3.4, the negative electric field of -0.5 Å^{-1} primarily enhances the H_2 adsorption energy for all metal-decorated SnX_2 systems. It is, therefore, expected that applying an external electric field can also increase the desorption temperature. When an external electric field of -0.5 eV Å^{-1} is applied, the desorption temperatures of hydrogen molecules on metal-decorated SnS_2 and $SnSe_2$ monolayers rise at all pressures, as shown in Table 6. This enhancement indicates that the field strengthens hydrogen adsorption by inducing dipole moments in the H_2 molecules, which improves their interaction with the metal-decorated monolayer. The increase in desorption temperature is more pronounced for Ca- and Mg-decorated systems, where stronger electrostatic interactions lead to greater field sensitivity. For example, in Ca-decorated SnS_2 at 10 MPa, the desorption temperature increases from 211 K to 226 K, while in $SnSe_2$, it rises from 209 K to 229 K.

In contrast, alkali metal-doped systems (Li, Na, K) show smaller temperature shifts, with K-decorated SnS_2 exhibiting a slight decrease in desorption temperature, suggesting a weaker influence of the electric field on these systems. This trend indicates that alkali metals, which already exhibit weaker charge transfer interactions, do not benefit as significantly from the applied field compared to alkaline-earth metals. The combination of higher pressure and an external electric field provides a synergistic effect, further stabilizing hydrogen adsorption. However, despite this improvement, desorption temperatures at moderate pressures (1 MPa) remain below the typical PEM fuel cell operating range (~233–473 K), indicating that while an external field enhances adsorption, additional modifications, such as co-doping or stronger fields, may be necessary for practical hydrogen storage applications. These findings demonstrate that external electric fields can serve as a tunable parameter to improve hydrogen storage stability in metal-decorated SnS_2 and $SnSe_2$ monolayers, providing a potential strategy for optimizing 2D materials for hydrogen storage technologies.

Table 6 Desorption temperatures in Kelvin for maximum H_2 molecules adsorbed on metal-decorated SnX_2 monolayer without (E_f = 0.0 V Å^{-1}) and with an electric field (E_f = -0.5 V Å^{-1}) at pressures (P) in MPa

	SnS_2			$SnSe_2$		
Metal	P = 0.1	P = 1	P = 10	P = 0.1	P = 1	P = 10
			E_f = 0.0 V Å^{-1}			
Li	115	139	174	104	125	157
Na	117	140	176	114	137	172
K	106	127	159	104	125	157
Mg	115	138	173	104	125	157
Ca	141	170	212	140	168	210
			E_f = -0.5 V Å^{-1}			
Li	122	146	184	109	132	165
Na	118	142	178	119	143	180
K	101	121	152	101	121	152
Mg	134	161	202	116	140	175
Ca	152	183	226	154	185	229

Conclusions

This study uses disperon-corrected DFT calculations to investigate hydrogen adsorption on SnS_2 and $SnSe_2$ monolayers decorated with alkali (Li, Na, K) and alkaline-earth (Mg, Ca) metals. The results demonstrate that metal decoration significantly enhances hydrogen adsorption capacity, with Ca exhibiting the strongest interaction and the ability to accommodate multiple hydrogen molecules. The adsorption energies primarily fall within the strong physisorption regime, balancing stability and desorption feasibility. The maximum gravimetric storage capacities range from 2.67 to 4.64 wt%.

The effects of temperature, pressure, and external electric fields were analyzed to assess the practical feasibility of hydrogen storage in these systems. Increasing pressure stabilizes hydrogen adsorption, with desorption temperatures at 10 MPa reaching the lower operational limits of PEM fuel cells (~233 K). Applying an external electric field (-0.5 V Å^{-1}) further enhances adsorption stability, increasing desorption temperatures by 10–20 K due to dipole-induced interactions. Despite these improvements, moderate-pressure conditions (1 MPa) remain insufficient for practical storage, suggesting that additional strategies such as co-doping, defect engineering, or stronger electric fields may be required to enhance adsorption strength. Although our results currently fall below the DOE gravimetric and operational targets, this study clearly demonstrates an effective route toward enhancing hydrogen adsorption performance through strategic metal decoration and external field tuning. The present findings thus provide valuable theoretical guidance for future studies aimed at

achieving or surpassing DOE hydrogen storage benchmarks. These findings demonstrate the tunability of metal-decorated SnX_2 monolayers for hydrogen storage and provide insights into their potential for future applications in clean energy technologies.

Conflicts of interest

The authors declare that they have no known competing financial interests or personal relationships that could have appeared to influence the work reported in this paper.

Data availability

All data supporting the findings of this study are available within the article and its supplementary information (SI). Supplementary information: (1) Phonon dispersion of SnS_2 and $SnSe_2$ monolayers. (2) Numerical values of binding energies and cohesive energies. (3) Atomic structure and charge difference of pristine and metal-decorated $SnSe_2$ and (4) *Ab-Initio* Molecular Dynamics (AIMD) simulations for single and multiple metal decoration. See DOI: **https://doi.org/10.1039/d5cp03873a**.

Acknowledgements

This work was supported by the NSRF *via* the Program Management Unit for Human Resources & Institutional Development, Research, and Innovation [grant number B39G670019]. A. S. is supported by the Faculty of Science, Kasetsart University, through thesis grant for publication. We thank the NSTDA Supercomputer Center (ThaiSC) for providing computing resources for this work.

References

1 S. E. Hosseini and M. A. Wahid, *Renewable Sustainable Energy Rev.*, 2016, **57**, 850–866.
2 L. Schlapbach and A. Züttel, *Nature*, 2001, **414**, 353–358.
3 T. Capurso, M. Stefanizzi, M. Torresi and S. M. Camporeale, *Energy Convers. Manage.*, 2022, **251**, 114898.
4 L. Mulky, S. Srivastava, T. Lakshmi, E. R. Sandadi, S. Gour, N. A. Thomas, S. Shanmuga Priya and K. Sudhakar, *Mater. Chem. Phys.*, 2024, **325**, 129710.
5 N. A. A. Rusman and M. Dahari, *Int. J. Hydrogen Energy*, 2016, **41**, 12108–12126.
6 A. Züttel, P. Sudan, P. Mauron, T. Kiyobayashi, C. Emmenegger and L. Schlapbach, *Int. J. Hydrogen Energy*, 2002, **27**, 203–212.
7 A. Züttel, *Mater. Today*, 2003, **6**, 24–33.
8 C. Ataca, E. Aktürk, S. Ciraci and H. Ustunel, *Appl. Phys. Lett.*, 2008, **93**, 043123.
9 V. Tozzini and V. Pellegrini, *Phys. Chem. Chem. Phys.*, 2013, **15**, 80–89.
10 P. Reunchan and S.-H. Jhi, *Appl. Phys. Lett.*, 2011, **98**, 093103.
11 S. Seenithurai, R. K. Pandyan, S. V. Kumar, C. Saranya and M. Mahendran, *Int. J. Hydrogen Energy*, 2014, **39**, 11016–11026.
12 Q. Yin, G. Bi, R. Wang, Z. Zhao and K. Ma, *Int. J. Hydrogen Energy*, 2023, **48**, 26288–26300.
13 T. Kaewmaraya, N. Thatsami, P. Tangpakonsab, R. Kinkla, K. Kotmool, C. Menendez, K. F. Aguey-Zinsou and T. Hussain, *Appl. Surf. Sci.*, 2023, **629**, 157391.
14 P. Netrattana and P. Reunchan, *J. Phys.: Conf. Ser.*, 2017, **901**, 012102.
15 M. Wu, Q. Wang, Q. Sun and P. Jena, *J. Phys. Chem. C*, 2013, **117**, 6055–6059.
16 A. Hashmi, M. U. Farooq, I. Khan, J. Son and J. Hong, *J. Mater. Chem. A*, 2017, **5**, 2821–2828.
17 N.-X. Qiu, Z.-Y. Tian, Y. Guo, C.-H. Zhang, Y.-P. Luo and Y. Xue, *Int. J. Hydrogen Energy*, 2014, **39**, 9307–9320.
18 L. Wang, X. Chen, H. Du, Y. Yuan, H. Qu and M. Zou, *Appl. Surf. Sci.*, 2018, **427**, 1030–1037.
19 Y. Wang, R. Zheng, H. Gao, J. Zhang, B. Xu, Q. Sun and Y. Jia, *Int. J. Hydrogen Energy*, 2014, **39**, 14027–14032.
20 R. Trivedi, S. Kaur, N. Garg and B. Chakraborty, *Appl. Surf. Sci.*, 2023, **622**, 156806.
21 G. Sanyal, H. T. Nair, P. K. Jha and B. Chakraborty, *J. Energy Storage*, 2023, **68**, 107892.
22 V. Mahamiya, J. Dewangan and B. Chakraborty, *Int. J. Hydrogen Energy*, 2024, **50**, 1302–1316.
23 A. Sripothongnack, W. Teeranattapong, A. Ananchuensook, T. Thanasarnsurapong, J. T-Thienprasert, C. Wongchoosuk and P. Reunchan, *Surf. Interfaces*, 2025, **56**, 105481.
24 M. Chen, H. Zhang, H. Li, Z. Zhao, K. Wang, Y. Zhou, X. Zhao and D. P. Dubal, *Coord. Chem. Rev.*, 2024, **503**, 215653.
25 A. Mondal and A. Vomiero, *Adv. Funct. Mater.*, 2022, **32**, 2208994.
26 D. Er, H. Ye, N. C. Frey, H. Kumar, J. Lou and V. B. Shenoy, *Nano Lett.*, 2018, **18**, 3943–3949.
27 E. W. Keong Koh, C. H. Chiu, Y. K. Lim, Y.-W. Zhang and H. Pan, *Int. J. Hydrogen Energy*, 2012, **37**, 14323–14328.
28 J. Cao, J. Zhou, Y. Zhang and X. Liu, *Microelectron. Eng.*, 2018, **190**, 63–67.
29 H. Liu, S. Yang, G. Lei, M. Xu, H. Xu, Z. Lan, Z. Wang, J. Xiong and H. Gu, *Int. J. Hydrogen Energy*, 2022, **47**, 12096–12106.
30 N. Song, Y. Wang, S. Ding, Y. Yang, J. Zhang, B. Xu, L. Yi and Y. Jia, *Vacuum*, 2015, **117**, 63–67.
31 K. Chaoui, H. Zaari, Z. Mansouri, F. Caballero-Briones, A. Benyoussef, A. El Kenz and A. Sibari, *J. Energy Storage*, 2025, **109**, 115110.
32 Z. D. Ponkiya and P. K. Jha, *Int. J. Hydrogen Energy*, 2025, **144**, 458–468.
33 X. Zhou, L. Gan, W. Tian, Q. Zhang, S. Jin, H. Li, Y. Bando, D. Golberg and T. Zhai, *Adv. Mater.*, 2015, **27**, 8035–8041.
34 A. Shafique, A. Samad and Y.-H. Shin, *Phys. Chem. Chem. Phys.*, 2017, **19**, 20677–20683.
35 A. Rahman, H. J. Kim, M. Noor-A-Alam and Y.-H. Shin, *Curr. Appl. Phys.*, 2019, **19**, 709–714.
36 J. M. Gonzalez and I. I. Oleynik, *Phys. Rev. B*, 2016, **94**, 125443.

 This journal is © the Owner Societies 2025

37 M. K. Butt, V. A. Dinh, H. M. Zeeshan, Z. Yang, S. Wang and K. Jin, *Mater. Sci. Semicond. Process.*, 2021, **136**, 106175.
38 F. Zhang, C. Xia, J. Zhu, B. Ahmed, H. Liang, D. B. Velusamy, U. Schwingenschlögl and H. N. Alshareef, *Adv. Energy Mater.*, 2016, **6**, 1601188.
39 S. Ratnaningsih, A. Azhar, A. B. Cahaya, E. Suprayoga and M. A. Majidi, *J. Phys.: Conf. Ser.*, 2022, **2377**, 012010.
40 D. Pang, P. Shi, L. Lin, K. Xie, C. Deng and Z. Zhang, *Phys. Chem. Chem. Phys.*, 2023, **25**, 6626–6635.
41 X. Wang and J. Wang, *Mater. Sci. Semicond. Process.*, 2021, **121**, 105416.
42 H. T. T. Nguyen, V. V. Tuan, C. V. Nguyen, H. V. Phuc, H. D. Tong, S.-T. Nguyen and N. N. Hieu, *Phys. Chem. Chem. Phys.*, 2020, **22**, 11637–11643.
43 S. Lee, M. Lee, H. Choi, D. S. Yoo and Y.-C. Chung, *Int. J. Hydrogen Energy*, 2013, **38**, 4611–4617.
44 T. He, H. Cao and P. Chen, *Acc. Mater. Res.*, 2021, **2**, 726–738.
45 W. Xu, Y. Zhou, S. Yang, G. Lei, W. Xie, M. Xu, J. Xiong and Z. Lan, *Int. J. Hydrogen Energy*, 2024, **83**, 226–235.
46 R. Varunaa and P. Ravindran, *Phys. Chem. Chem. Phys.*, 2019, **21**, 25311–25322.
47 Y. S. Al-Hamdani, A. Zen, A. Michaelides and D. Alfè, *Phys. Rev. Mater.*, 2023, **7**, 035402.
48 G. Kresse and J. Furthmüller, *Comput. Mater. Sci.*, 1996, **6**, 15–50.
49 G. Kresse and J. Furthmüller, *Phys. Rev. B: Condens. Matter Mater. Phys.*, 1996, **54**, 11169–11186.
50 J. P. Perdew, K. Burke and M. Ernzerhof, *Phys. Rev. Lett.*, 1996, **77**, 3865–3868.
51 S. Grimme, J. Antony, S. Ehrlich and H. Krieg, *J. Chem. Phys.*, 2010, **132**, 154104.
52 S. Grimme, *J. Comput. Chem.*, 2006, **27**, 1787–1799.
53 E. Caldeweyher, J.-M. Mewes, S. Ehlert and S. Grimme, *Phys. Chem. Chem. Phys.*, 2020, **22**, 8499–8512.
54 A. Tkatchenko and M. Scheffler, *Phys. Rev. Lett.*, 2009, **102**, 073005.
55 D. Henwood and J. D. Carey, *Phys. Rev. B: Condens. Matter Mater. Phys.*, 2007, **75**, 245413.
56 J. Wong, S. Yadav, J. Tam and C. Veer Singh, *J. Appl. Phys.*, 2014, **115**, 224301.
57 I. Souza, J. Íñiguez and D. Vanderbilt, *Phys. Rev. Lett.*, 2002, **89**, 117602.
58 H. Zhang, C. Xia, X. Zhao, T. Wang and J. Li, *Appl. Surf. Sci.*, 2015, **356**, 1200–1206.
59 A. N. Sosa, B. J. Cid, Á. Miranda, L. A. Pérez, G. H. Cocoletzi and M. Cruz-Irisson, *J. Energy Storage*, 2023, **73**, 108913.
60 Y. Zhou, W. Chu, F. Jing, J. Zheng, W. Sun and Y. Xue, *Appl. Surf. Sci.*, 2017, **410**, 166–176.
61 J. Dewangan, V. Mahamiya, A. Shukla and B. Chakraborty, *Int. J. Hydrogen Energy*, 2023, **48**, 37908–37920.
62 X. Zhang, J. Hao, S. Gao, L. Wu, G. Wu, F. Chen, L. Gao and P. Lu, *Int. J. Quantum Chem.*, 2022, **122**, e26997.
63 S. Kaviani, I. Piyanzina, O. V. Nedopekin and D. A. Tayurskii, *Int. J. Hydrogen Energy*, 2023, **48**, 30069–30084.
64 D. B. Putungan, S.-H. Lin, C.-M. Wei and J.-L. Kuo, *Phys. Chem. Chem. Phys.*, 2015, **17**, 11367–11374.
65 J. Zhou, J. Cao, J. Shi, Y. Zhang, J. Chen, W. Wang and X. Liu, *Nanoscale Res. Lett.*, 2020, **15**, 102.
66 S. Yang, S. Xie, L. Tan, G. Lei, H. Xu, Z. Lan, Z. Wang and H. Gu, *Int. J. Hydrogen Energy*, 2022, **47**, 29579–29591.
67 J. Zhou, Q. Wang, Q. Sun, P. Jena and X. S. Chen, *Proc. Natl. Acad. Sci. U. S. A.*, 2010, **107**, 2801–2806.
68 M. W. Chase and N. I. S. Organization, *NIST-JANAF thermochemical tables*, American Chemical Society, Washington, DC, 1998.
69 C. Drawer, J. Lange and M. Kaltschmitt, *J. Energy Storage*, 2024, **77**, 109988.
70 E. Ogungbemi, T. Wilberforce, O. Ijaodola, J. Thompson and A. G. Olabi, *Int. J. Energy Res.*, 2021, **45**, 1227–1245.